Nanoscale Advances

ROYAL SOCIETY OF CHEMISTRY

PAPER

View Article Online
View Journal | View Issue

Cite this: *Nanoscale Adv.*, 2022, **4**, 190

The synthesis of a nanodrug using metal-based nanozymes conjugated with ginsenoside Rg3 for pancreatic cancer therapy†

Xiaoxiong Zhao,‡[ab] Jicheng Wu,‡[cd] Kaixin Zhang,[cd] Danjing Guo,[e] Liangjie Hong,[e] Xinhua Chen,[be] Ben Wang*[cd] and Yujun Song *[ab]

Nanozymes have limited applications in clinical practice due to issues relating to their safety, stability, biocompatibility, and relatively low catalytic activity in the tumor microenvironment (TME) *in vivo*. Herein, we report a synergistic enhancement strategy involving the conjugation of metal-based nanozymes ($Fe@Fe_3O_4$) with natural bioactive organic molecules (ginsenoside Rg3) to establish a new nanodrug. Importantly, this metal–organic nanocomposite drug ensured the stability and biosafety of the nanozyme cores and the cellular uptake efficiency of the whole nanodrug entity. This nanodrug is based on integrating the biological characteristics and intrinsic physicochemical properties of bionics. The glycoside chain of Rg3 forms a hydrophilic layer on the outermost layer of the nanodrug to improve the biocompatibility and pharmacokinetics. Additionally, Rg3 can activate apoptosis and optimize the activity and status of normal cells. Internal nanozymes enter the TME and release Fe^{3+} and Fe^{2+}, and the central metal Fe(0) continuously generates highly active Fe^{2+} under the conditions of the TME and in the presence of Fe^{3+}, maintaining the catalytic activity. Therefore, these nanozymes can effectively produce reactive oxygen species and oxygen in the TME, thereby promoting the apoptosis of cancer cells. Thus, we propose the use of a new type of metal–organic nanocomposite material as a synergistic strategy against cancer.

Received 21st September 2021
Accepted 20th October 2021

DOI: 10.1039/d1na00697e

rsc.li/nanoscale-advances

Introduction

Compared with natural enzymes, nanozymes have been rapidly developed for use in biosensing, antibacterial resistance, and immunoassay because they possess high stability, low cost, and are easy to prepare.[1–5] In the unique physiological microenvironment, tumor cells produce a large concentration of hydrogen peroxide (H_2O_2) *via* the overexpression of superoxide dismutase (SOD) from the mitochondria. Nanozymes have shown promise in reactive oxygen species (ROS)-mediated tumor therapy.[6,7] Several nanozymes for efficient tumor therapy and/or precise imaging diagnosis have been developed, such as carbon-based nanoparticles (NPs), metal NPs, and metal oxide NPs, all of which participate in unique catalytic activities.[4,8,9]

Iron-based NPs (*e.g.*, FeO_x) have attracted great interest.[10,11] First, magnetic resonance imaging mediated by iron-based NPs has become mature, thereby providing a foundation for an integrated platform for diagnosis and treatment.[12] Second, in the research field of photothermal therapy, iron compound-based NPs perform a pivotal role due to their high heat conversion efficiency.[13,14] Finally, iron-based nanomaterials can engage in catalytic functions such as dual enzyme peroxidase (POD)- and catalase (CAT)-like activities.[9,15,16] According to previous studies, there is higher POD-like activity under acidic conditions for iron-based nanomaterials, and they catalyze H_2O_2 to generate highly toxic ROS, while under neutral conditions, higher CAT-like activity has been observed, with catalysis of H_2O_2 to generate H_2O and O_2.[15] Using this method, a highly toxic ROS kills tumor cells, and O_2 can control tumor hypoxia, reduce the antioxidant capacity of tumor cells, strengthen the effect of oxidative damage, and inhibit tumor invasion and migration.[17,18]

Pancreatic cancer is a highly malignant disease characterized by local invasion and metastasis, and is the deadliest among all cancers.[19] In terms of patient survival, most patients

[a]*Center for Modern Physics Technology, School of Mathematics and Physics, University of Science and Technology Beijing, Beijing 100083, China. E-mail: songyj@ustb.edu.cn*
[b]*Zhejiang Key Laboratory for Pulsed Power Technology Translational Medicine, Hangzhou 310000, China*
[c]*Cancer Institute, Key Laboratory of Cancer Prevention and Intervention, China National Ministry of Education, The Second Affiliated Hospital, Zhejiang University School of Medicine, Hangzhou 310009, China*
[d]*Institute of Translational Medicine, Zhejiang University, Hangzhou 310029, China*
[e]*Key Laboratory of Combined Multi-Organ Transplantation, Ministry of Public Health, Department of Hepatobiliary and Pancreatic Surgery, The First Affiliated Hospital, Zhejiang University School of Medicine, Hangzhou 310003, China*

† Electronic supplementary information (ESI) available. See DOI: 10.1039/d1na00697e

‡ These authors contributed equally to this work.

have advanced disease at diagnosis with a poor prognosis, and the 5 year survival rate is less than 5%.[20] Additionally, many patients are inoperable because of metastasis and invasion.[21] Instead of surgical resection, chemotherapy has become the standard treatment for locally metastatic or advanced tumors. Unfortunately, the current chemotherapy drugs and regimens, including gemcitabine, 5-fluorouracil (FU), oxaliplatin, and nab-paclitaxel cause obvious side effects and chemoresistance, resulting in the inability to effectively inhibit tumor growth.[22] Therefore, there is an urgent need to develop new methods for treating pancreatic cancer, such as the development of new nanodrugs.

The development of new nanodrugs with high efficiency, high safety, high biocompatibility, and longer residence time (with improved drug utilization) is currently a major difficulty. There are several issues regarding the clinical treatment of pancreatic cancer using nano-metalloenzymes (NMEs). First, the stability of NMEs is problematic. In addition to the double enzymatic activities, iron-based NMEs can catalyze various biochemical reactions, and this may have unexpected biological effects in a complex *in vivo* microenvironment.[23] Safety is also an issue, because the premature leakage of catalytic iron ions may cause toxic effects in normal cells and/or tissues, and may cause severe collateral damage.[24] Therefore, the composition, microstructure, delivery process, and surface modification of NMEs must be optimized for increased efficiency, stability, and biocompatibility.

Ginsenosides are effective therapeutic ingredients with multiple pharmacologic activities and have been widely used in clinical practice.[25] Ginsenoside Rg3 (Rg3) exhibits anticancer properties, promotes tumor cell apoptosis, inhibits tumor infiltration, proliferation, and angiogenesis, and reduces the recurrence of cancer metastasis.[26,27] Studies have shown that the combination of Rg3 and commonly used chemotherapeutics such as paclitaxel, docetaxel, cisplatin, and doxorubicin significantly increased the therapeutic effect and reduced toxicity.[28,29] It has also been observed that Rg3 is effective in reshaping the immunomodulatory effect of the tumor microenvironment (TME).[30,31] However, most drugs are directly metabolized by the kidneys after entering the human body, and therefore, the bioavailability of Rg3 is very low, with only a tiny concentration reaching the tumor site.[32,33]

Herein, we report a new type of nanodrug (RNME) synthesized by the bioactive organic molecule (Rg3) coupled with NME ($Fe@Fe_3O_4$). RNME confers the anticancer effects of NME and Rg3 and has overcome their individual shortcomings with obvious synergistic effects. The center $Fe@Fe_3O_4$ NME exhibits excellent biocatalytic activity and imaging functions.[34] The innermost metal Fe^0, due to weak acid conditions and the presence of Fe^{3+} in the TME, will continue to generate high catalytic activity of Fe^{2+}. Therefore, these NMEs can effectively produce ROS and oxygen, promoting the apoptosis of cancer cells.[35]

These types of NMEs have been used to treat hepatocellular carcinoma, and they can significantly inhibit liver cancer progression and lung metastasis.[36] The outer layer of Rg3 contains a hydrophilic glycoside chain that can form a hydrophilic layer on the outer layer of the drug, which increases biocompatibility and ensures stability and catalytic activity of the internal NME. It also increases the safety of the RNME, and prevents toxic side effects. Rg3 also regulates the accumulation of lipids and induces the formation of the second phase, thereby significantly affecting the pharmacokinetics in the body.[32] This results in prolonged blood circulation of the new nanodrug, leading to a greater amount of the high-concentration nanodrug reaching the tumor site, accelerating endocytosis, and solving the problem of the low transport efficiency of Rg3 alone.

In this study, RNME was used in the treatment of pancreatic cancer *in situ*. The application of RNME can safely and effectively inhibit the development of pancreatic cancer and effectively prevent the metastasis of pancreatic cancer to the liver. This study highlights the synergistic anti-tumor potential of the combination of Rg3 and NMEs. Also, a new perspective to explore similar synergistic treatment strategies using novel metal–organic nanocomposites is discussed.

Results and discussion

Synthesis process and characterization of NPs and NMEs

$Fe@Fe_3O_4$ NPs were synthesized using a simple programmed microfluidic process.[37–40] Fig. 1A and S1† show transmission electron microscopy (TEM) images of $Fe@Fe_3O_4$ NPs. They present with slight agglomeration due to the magnetic dipole attraction of the magnetic NPs. The HRTEM image of the $Fe@Fe_3O_4$ NPs reveal a clear core–shell structure with amorphous cores and tiny crystalline parts doped in the shell. The X-ray diffraction (XRD) of NPs (Fig. 1B) clearly shows two different crystal structures, including a core of typical amorphous Fe and shells of crystalline magnetite Fe_3O_4 (PDF 79-0419). The formation of self-oxide shells assists in stabilizing the magnetic Fe core components and increasing biocompatibility, which is beneficial for conjugation between the surface Fe ions and Rg3. Then, our previously developed method was used to synthesize RNME *via* modification with a double silane coupling agent and the activation of the amino group using a crosslinking agent.[34,41] In addition, the coupling efficiency of Rg3 and NPs is shown in Fig. 1C. When the mass ratio was 1 : 1, most active groups on the surface of the NPs were coupled with Rg3, and the coupling efficiency was significantly reduced after increasing the amount of Rg3. Hence, the 1 : 1 mass ratio can be used for all subsequent works.

Fig. 1D and S2† depict the TEM images of RNME. Compared with simple NPs, RNME significantly increased the concentration of organic matter on the surface of NPs and resulted in a more evident aggregation. This phenomenon is mainly attributed to the NPs themselves, which are magnetic and easily cause agglomeration. Additionally, the coupling reaction generated during the conjugation process results in obvious NP aggregation, which also indirectly confirms the success of the conjugation. Compared with NPs, the HRTEM image of RNME shows a significant organic coating, and thus, the RNME image is not as straightforward as that of simple NPs.

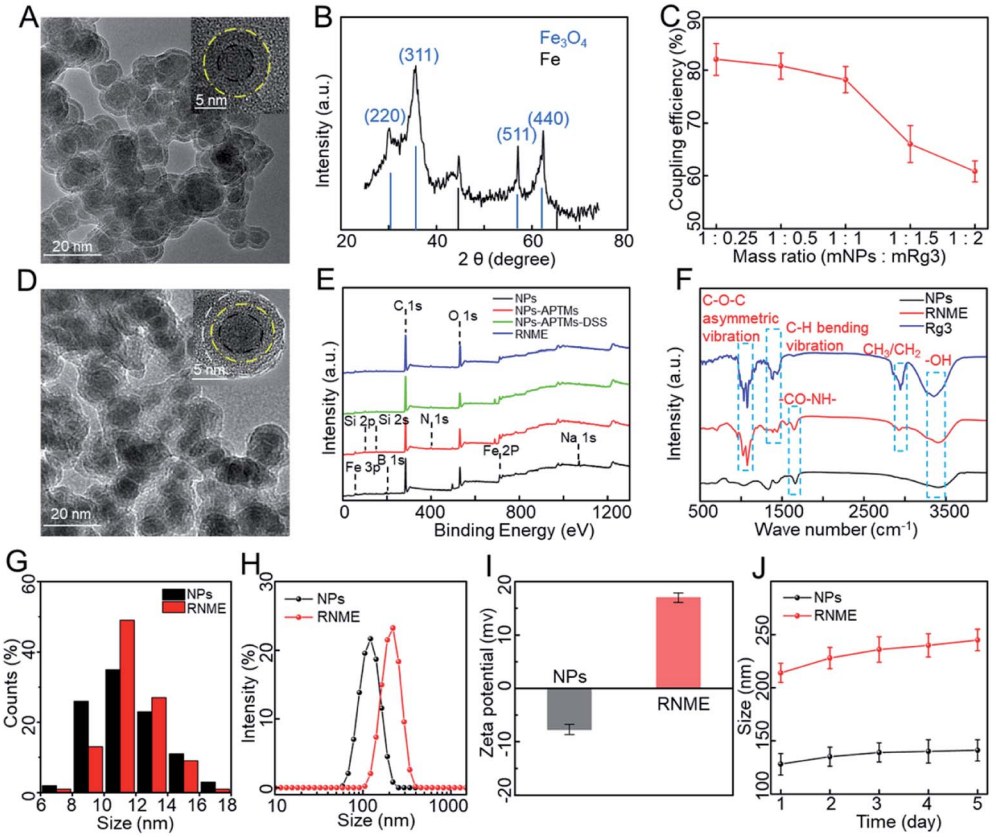

Fig. 1 The characteristics of NPs and RNME. (A) A TEM image of Fe@Fe_3O_4. (B) The XRD pattern of Fe@Fe_3O_4. (C) The coupling efficiency at different mass ratios (mNPs : mRg3). (D) A TEM image of RNME. (E) XPS spectra from each step in the synthesis process. (F) FT-IR spectra of Fe@Fe_3O_4, Rg3, and RNME. (G) A histogram of the size distributions of Fe@Fe_3O_4 and RNME. (H) The hydrodynamic sizes of Fe@Fe_3O_4 and RNME. (I and J) Zeta potential and stability data for Fe@Fe_3O_4 and RNME.

To further assess the coupling process, X-ray photoelectron spectroscopy (XPS) and Fourier transform infrared (FT-IR) spectroscopy were used to characterize different samples. Compared with pure NPs, the XPS of each synthesis step (Fig. 1E and Table S1†) showed that new peaks of Si and N were identified in the modified NPs. The elements Si and N were derived from modified APTMS, thereby confirming the modification of –OH to –NH_2 on the surface of NPs. Compared with pure NPs and Rg3, the FT-IR spectroscopy of RNME (Fig. 1F) revealed that RNME contains the characteristic peak –CO–NH– of pure NPs, and characteristic peaks for C–O–C asymmetric vibration, C–H bending vibration, and CH_3/CH_2 of the pure Rg3.

A statistical analysis based on NPs and RNME by randomly selecting 200 NPs showed that their average diameters were 11.5 ± 1.0 and 12.7 ± 1.0 nm, respectively, as shown in Fig. 1G. Then, the hydrodynamic diameter, zeta potential, and stability of RNME were evaluated. The hydrodynamic diameters of simple NPs and RNME are approximately 128 and 214 nm, respectively (Fig. 1H). Due to the existence of several hydroxyl groups on the surface of simple NPs, they exhibited a negative potential. However, due to the presence of amino groups during subsequent processes, there was a significant positive potential for RNME that facilitated its entrance into cells to reach the mitochondria (Fig. 1I).[42] To confirm the stability of simple NPs and RNME, the hydrodynamic diameter was evaluated at the same time every day for 5 days. As shown in Fig. 1J, simple NPs and RNME exhibited excellent stability and minimal change in hydrodynamic diameter. Combined analyses revealed that RNME was successfully synthesized by the method according to the proposed coupling reaction mechanism.

Assessment of the release mechanism of NPs and RNME *in vitro*

The CAT- and POD-like activities of RNME were investigated *in vitro* (Fig. 2A). First, whether simple NPs or RNME possess CAT-like activity under acidic conditions was investigated, and the generation of O_2 in the presence of H_2O_2 and NPs or RNME was evaluated. Notably, a simple H_2O_2 group did not significantly differ over time. After adding NPs and RNME, a large amount of O_2 molecules was produced over time (Fig. 2B). Compared with simple NPs, the same mass of RNME contained 60% NPs, and the reaction with H_2O_2 exhibited a significant distinct hysteresis due to encapsulation by organic molecules. Simple NPs and RNME exhibited excellent CAT-like activity, which effectively catalyzed H_2O_2 to generate O_2 molecules. Furthermore, under hypoxic conditions, the invasion and migration capacity of tumor cells increased, and the antioxidant capacity was enhanced. Therefore, changing the hypoxic state of the tumor

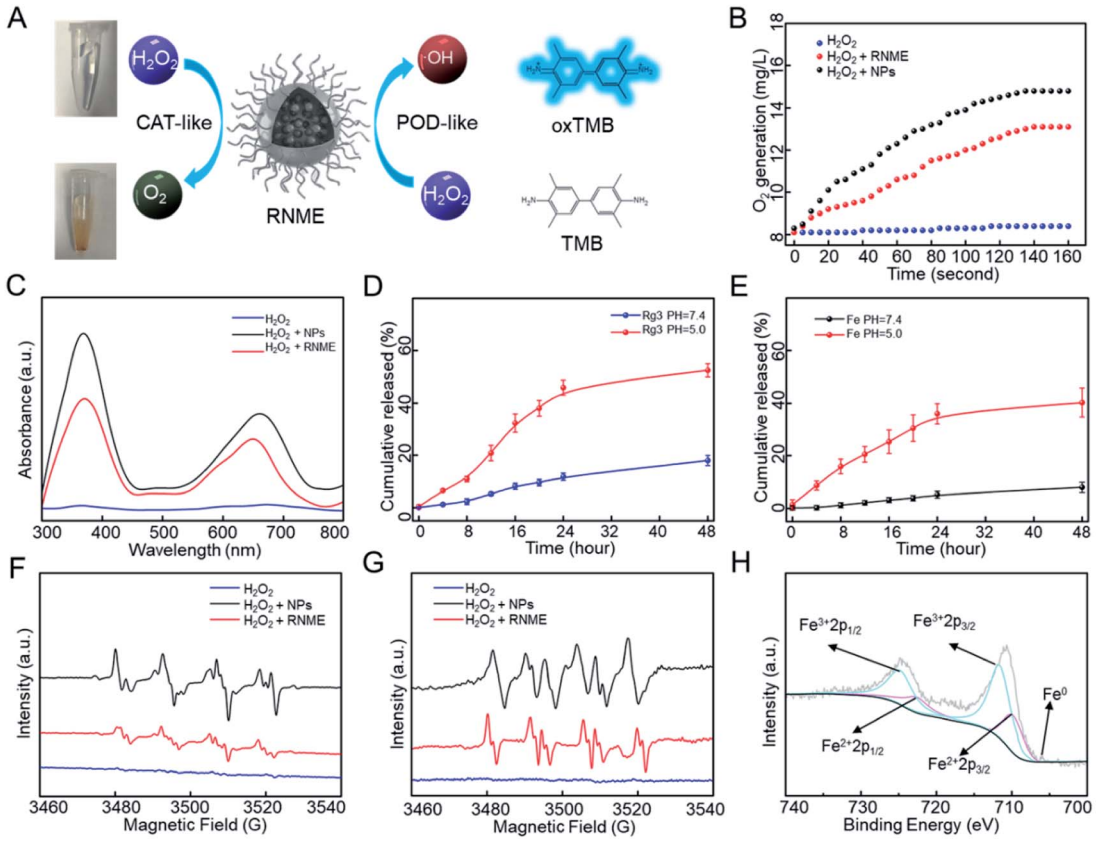

Fig. 2 The responsiveness and catalytic mechanism of RNME. (A) A diagram of the CAT- and POD-like activities. (B) The production of O_2 after incubation with Fe@Fe_3O_4 and RNME. (C) UV-Vis absorption spectra of TMB after incubation with Fe@Fe_3O_4 and RNME. (D) Rg3 release rates from RNME at various time intervals *via* HPLC analysis. (E) Iron release rates from RNME at different time intervals *via* ICP assays. (F and G) ESR spectra of $^{\bullet}OH$ and $O_2^{\bullet-}$ spin after incubation with Fe@Fe_3O_4 and RNME. (H) A high-resolution scan showing the Fe 2p XPS spectrum of Fe@Fe_3O_4.

site may decrease the invasion and migration of tumor cells, reduce the antioxidant capacity of tumor cells, and enhance the effects of oxidative damage.[17]

Then, the POD-like activities of NPs and RNME were investigated *via* the oxidation of 3,3′,5,5′-tetramethylbenzidine (TMB) in the presence of H_2O_2. UV–Vis absorption spectroscopy was used to monitor the production of oxidized TMB. In the presence of H_2O_2 alone, the absorbance was negligible, which indicates that there was no oxidation reaction in the mixture of TMB and H_2O_2. However, when NPs and RNME were added to the mixed solution of TMB and H_2O_2 for 10 min, two prominent absorption peaks appeared at 370 and 652 nm in the UV-Vis absorption spectrum, which were attributed to oxidized TMB. Thus, NPs and RNME have the ability to catalyze H_2O_2 to produce ROS (Fig. 2C), and calculations based on the coupling efficiency indicate that the same mass of RNME contains approximately 60% NPs, confirming that the coupling of Rg3 did not reduce the catalytic activity of NPs.

Fe@Fe_3O_4 NPs participate in pH-dependent ionization. Fe ions are barely released at neutral pH, but sufficient release is achieved *via* acid hydrolysis in the TME.[43,44] Rg3 are more effectively degraded and transformed under acidic conditions than in neutral environments.[32] When Fe ions and Rg3 are hydrolyzed or degraded under acidic conditions, separation of the NPs and the organic pharmaceutical ingredients results.

Two characterization methods were used to assess RNME release behavior under different conditions. First, the release of Rg3 was used to investigate the release behavior of RNME at different pH levels. Next, the same amount of RNME supernatant was obtained at different time points for high-performance liquid chromatography (HPLC). RNME was extremely stable at neutral pH, and the amount of Rg3 in the solution was low. However, at pH 5.0, approximately 52.5% of Rg3 was released after 48 h, which confirmed the sensitivity of the material to the TME (Fig. 2D). After incubation of RNME in phosphate-buffered saline (PBS, pH 5.0 and 7.4) at different time points, the iron concentration in the supernatant was determined *via* inductively coupled plasma mass spectrometry (ICP-MS) (Fig. 2E) to further validate the sensitivity of RNME to the TME. We determined that Rg3-sheltered NME was specific to TME. Due to the relatively high blood pH (7.4), RNME remained inert during circulation. Therefore, after intravenous injection, the circulation time in the plasma can be prolonged. Eventually, more RNME reaches the tumor site under the action of electron paramagnetic resonance (EPR), which is conducive to the

specific release of the drug in cancer cells, and prevents toxic side effects.

To validate the catalytic mechanism and further identify the generated ROS, electron spin resonance (ESR) spectroscopy findings were used as discriminatory evidence for the generated ROS. Then, 5,5-dimethyl-1-pyrroline-*N*-oxide was utilized as a capture probe for $^{\bullet}OH$ and $O_2^{\bullet-}$. The ESR intensities obtained after a 3 min reaction with NPs and RNME are presented in Fig. 2F and G. The results showed that simple H_2O_2 did not exhibit ESR intensity, although the NPs and RNME showed prominent ESR intensity. Compared with simple H_2O_2, the $^{\bullet}OH$ radicals were characterized by a 1 : 2 : 2 : 1 signal. Then, the addition of NPs and RNME within 3 min induced a large amount of $^{\bullet}OH$. Hyperfine splitting into six peaks is characteristic of the $O_2^{\bullet-}$ radical, and the results showed that the NPs and RNME catalyzed H_2O_2 to produce a large amount of $O_2^{\bullet-}$. In addition, the chemical state of RNME was assessed using XPS. Specifically, the corresponding high-resolution XPS spectrum of Fe 2p (Fig. 2H) contained $2p_{1/2}$ and $2p_{3/2}$ parts of Fe^{3+} and Fe^{2+} due to spin–orbit splitting. In addition, the Fe^0 peak was near 706 eV. This information, along with the XRD results, strongly confirmed the successful synthesis of metal and metal oxide heterostructures. The weaker peak intensity was caused by the weaker penetration capability of XPS itself.

Based on the above data and results, a possible catalytic mechanism of RNME was proposed. First, when RNME enters the cell to decompose, due to the weak acid of the TME, the POD-like catalytic activity of the RNME was dominant. Fe^{2+} reacted with H_2O_2 to generate a large amount of $^{\bullet}OH$ (Fig. 2F). However, the above results also confirmed the existence of $O_2^{\bullet-}$ and O_2 (Fig. 2B and G), indicating that the CAT-like catalytic activity of RNME also played a part. After entering the cell, exposed Fe^{3+} reacted with H_2O_2 to form $O_2^{\bullet-}$, and then Fe^{3+} reacted with $O_2^{\bullet-}$ to form O_2.[15,35] However, due to the inhibition of the TME on the catalytic activity of CAT, only a portion of $O_2^{\bullet-}$ was converted to form O_2. In addition, the 48 hour release of RNME was approximately 50% (Fig. 2D and E), which was sufficient to achieve the effect of sustained drug release for long-term effectiveness. When a portion of iron ions was released, Rg3 and NPs were completely separated under the TME, lysosomes, and enzymes. Catalytic activity was still measured for the Fe@Fe_3O_4 NPs that remained intact. Fe^0 in the core of the NPs could be exposed and released, and in the presence of weak acid and Fe^{3+}, it was converted to Fe^{2+}, which continuously promotes the Fenton reaction.

Cytotoxicity of NPs and RNME

First, ICP-MS was used to assess the efficiency of endocytosis. Fig. 3A shows that NPs and RNME were sufficiently internalized. Then, the anticancer efficacy and biosafety of NPs and RNME were evaluated *via* Cell Counting Kit-8 (CCK-8) assay and the use of Rg3 as a positive control. NPs and RNME at different concentrations were incubated with pancreatic cancer cells (L3.6pl) for 24 h. As shown in Fig. 3B, NPs and RNME were slightly cytotoxic to cells at concentrations ranging from 0 to 400 μg mL^{-1}, thereby revealing that the biocompatibility of NPs and RNME is satisfactory. The cellular uptake results based on ICP-MS revealed that cytotoxicity was caused by the phagocytosis of NPs and RNME by L3.6pl cancer cells. In addition, when incubated with H_2O_2 or at a pH of 6.5 for 24 h, no cytotoxicity was measured in L3.6pl cells (Fig. S3†), which was attributed to the fact that the overexpression of H_2O_2 and weak acid can provide sufficient TME for the growth of L3.6pl. Because of the specific sensitivity to the TME by the NPs and RNME, the *in vitro* antitumor effect of NPs and RNME simulated under the TME state was investigated. The cell viability tests using L3.6pl cells incubated with NPs and RNME for 24 h exhibited evident concentration gradient cytotoxicity (Fig. 3C). In contrast, the cytotoxicity of the Rg3 groups was significantly lower than that of the NP and RNME groups. A fluorescent probe (2′,7′-dichlorofluorescin diacetate, DCFH-DA) was used to measure intracellular ROS levels to validate ROS production.

Flow cytometry (Fig. 3D) revealed that cells incubated with NPs and RNME showed remarkable DCF fluorescence intensity due to the production of a large amount of ROS *via* H_2O_2 catalysis by NPs and RNME. As shown in Fig. 3E, based on a quantitative analysis of ROS in cells that underwent different treatments, when compared with the control group, the Rg3, NPs, and RNME increased by 1.2, 4.7, and 4.8 times, respectively. It was confirmed that at the cellular level, RNME was more easily endocytosed by cells due to the modification of Rg3 and the positive potential, resulting in RNME only containing 60% of NPs, and still exerting an excellent catalytic H_2O_2 effect. The live/dead assay incorporated calcein-AM (green) and propidium iodine (PI) (red), and the ROS assay utilized Hoechst (blue) and DCFH-DA (green), as shown in Fig. 3F. Cells treated with NPs and RNME exhibited a significant increase in green DCF fluorescence, as shown in the CLSM image, compared with the control and Rg3 groups.

Due to the high migration and invasion ability of the L3.6pl cells, trans-well assays were performed (Fig. S4 and S5†). Rg3 alone slightly inhibited the invasion and migration of L3.6pl cells, and NPs and RNME significantly decreased the migration and invasion capabilities of L3.6pl cells.

Intracellular mechanism verification of NPs and RNME

Next we evaluated the intracellular action mechanism of NPs and RNME. First, detection kits (Annexin V-FITC/PI) were used to investigate apoptosis mechanisms (Fig. 4A and S6†). A higher level of apoptosis was detected in L3.6pl cells treated with RNME compared with cells separately treated with Rg3 or NPs, which further confirmed their synergistic effects.

Reduced glutathione (GSH) is a major intracellular antioxidant that is catalyzed by glutathione peroxidase 4 (GPX4) to become oxidized glutathione (GSSG) and reduce ROS to nontoxic hydroxyls. The concentrations of GSH and GSSG in L3.6pl cells were further investigated using different incubation methods based on the approach described in the GSH and GSSG assay kits. As shown in Fig. 4B, the NPs and RNME catalyzed H_2O_2 to generate ROS. GSH acts as an antioxidant to scavenge free radicals and convert them into GSSG, resulting in a significant decrease in the concentration of GSH/GSSG. GPX4

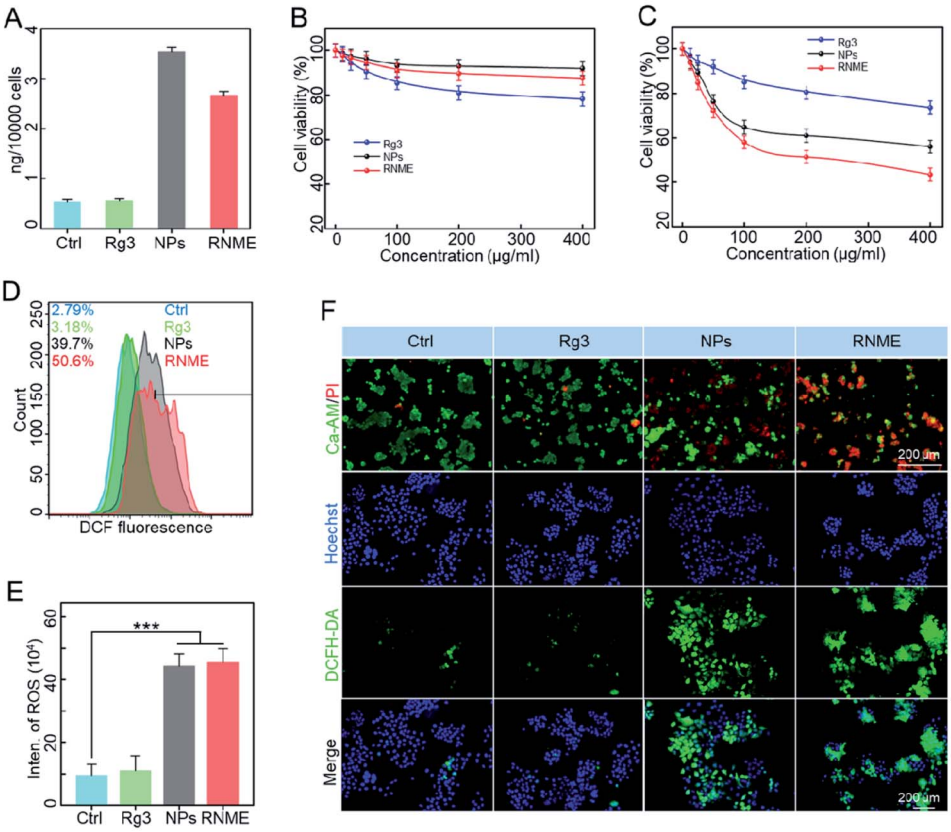

Fig. 3 Cytotoxicity of NPs and RNME in cancer cells. (A) ICP-MS analysis of the iron content in L3.6pl cells after incubation in different media. (B) Cell viability of L3.6pl cells after incubation with different treatments in a normal microenvironment. (C) Viability of L3.6pl cells after incubation with different treatments in the TME. (D) Flow cytometry analysis with DCFH-DA staining revealing intracellular ROS levels in L3.6pl cell lines subjected to different drug treatments. (E) Quantitative analysis of DCFH-DA staining *via* flow cytometry after treatment with different drugs. (F) CLSM images of L3.6pl cells co-stained with calcein-AM/PI and DCFH-DA/Hoechst.

and GSH are considered to be typical indicators that can be used to confirm the occurrence of ferroptosis. Therefore, GPX4 was chosen as the reactive protein of ferroptosis to compare different drugs.[45] Interestingly, the expression levels of GPX4 in the cells treated with RNME and NPs were significantly lower than those in other groups (Fig. S7†). This indicates that RNME has great potential in promoting oxidative stress and ferroptosis.

Beyond their role in energy metabolism *via* ATP production, the mitochondria are key organelles involved in regulating the cellular redox balance and intracellular apoptosis signaling, and thus, they can be used to determine cell viability and function in all tissues. In particular, the loss of mitochondrial integrity and function is considered a key cause of cell redox imbalance. Mitochondrial function is evaluated by monitoring oxygen consumption using a Seahorse analyzer. As shown in Fig. 4C and S8,† the NP and RNME groups decreased basal respiration and maximum respiration and the production of ATP. This indicates that the mitochondrial function and the integrity of the mitochondrial membrane in the NP and RNME groups was damaged. Furthermore, combined with its catalytic mechanism, the generation of ROS leads to lipid peroxidation (LPO), which destroys the membrane function of the mitochondria and affects metabolic pathways. We used C11-BODIPY and JC-1 dyes to evaluate the level of LPO and the integrity of mitochondrial membranes. C11-BODIPY staining showed that exposure of cells to NPs and RNME caused a significant increase in green fluorescence. This finding clearly indicates that NPs and RNME can activate LPO and cause damage to the mitochondrial membrane (Fig. 4D). JC1 staining revealed that when treated with PBS or Rg3, the cells emitted strong red fluorescence (JC-1 aggregates) in the mitochondria, which indicated that the mitochondria remained intact. In contrast, cells treated with NPs and RNME produced weak red and strong green fluorescence (JC-1 monomer), indicating an impaired mitochondrial membrane potential (Fig. 4E). These data confirmed that after NPs and RNME were endocytosed by cancer cells, a large amount of ˙OH was produced under the TME, leading to the accumulation of intracellular ROS. Then, ROS entered the cell nuclei to damage DNA and cause apoptosis, and they also caused LPO to damage mitochondria, resulting in ferroptosis. Rg3 in RNME can also activate apoptosis, thereby leading to cancer cell death under multiple actions.

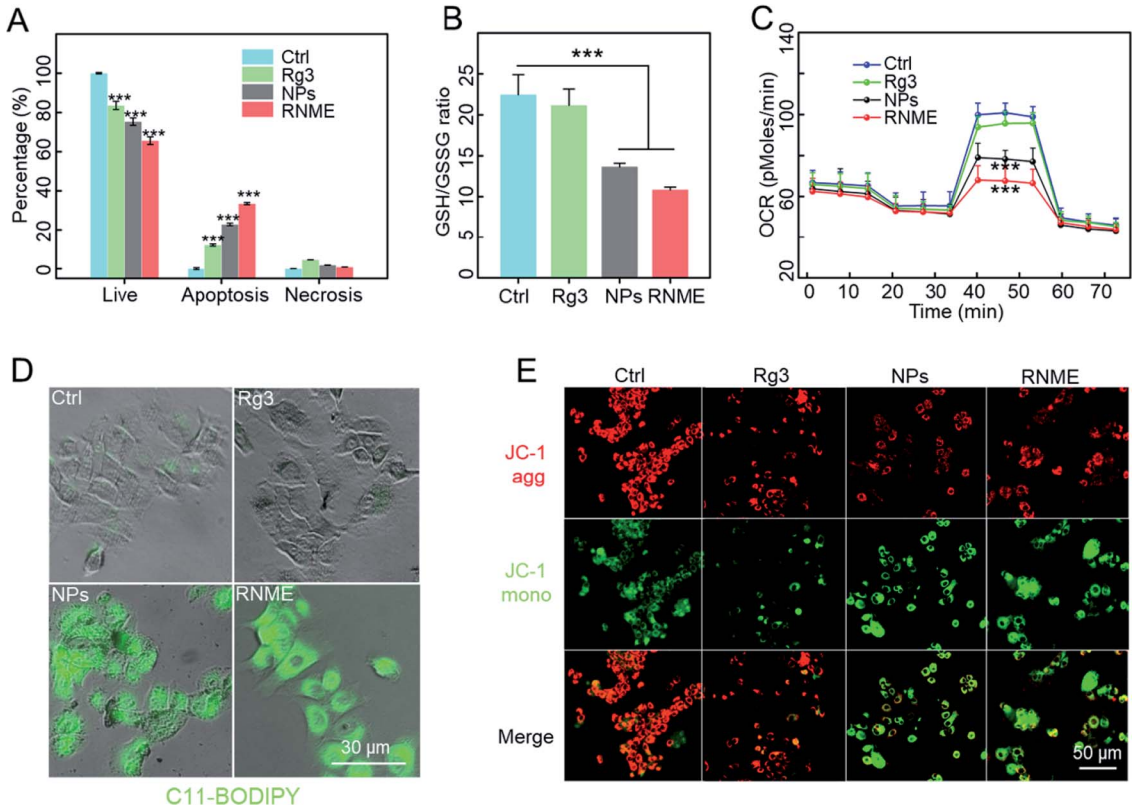

Fig. 4 Intracellular mechanism verification of NPs and RNME. (A) Quantitative analysis of Annexin V-FITC/PI apoptosis detection after treatment with different drugs. (B) GSH/GSSH ratios in L3.6pl cells after treatment with different drugs. (C) Seahorse XF24 extracellular fluid analysis revealing the oxygen consumption rate of mitochondrial function in L3.6pl cells after treatment with different drugs. (D) CLSM images of L3.6pl cells stained with C11-BODIPY. (E) CLSM images of L3.6pl cells stained with JC-1. All data are expressed as mean ± SD.

Therapeutic effects of RNME for *in situ* pancreatic cancer

Based on the outstanding *in vitro* anticancer activity, the *in vivo* therapeutic efficiency of RNME was further evaluated in detail. The antitumor therapeutic effects of Rg3, NPs, and RNME in an orthotopic nude mouse pancreatic ductal adenocarcinoma (PDAC) model were tested. First, to prove that RNME can effectively extend blood circulation in the body, the pharmacokinetics of RNME were examined. HPLC and ICP-MS were used to test the concentration of Rg3 and iron ions in the serum, respectively. It was found that simple NPs and Rg3 were quickly cleared in the blood. In contrast, RNME caused the significant effect of prolonging its circulation in the blood (Fig. 5A and B). The main reason for this was the presence of an outermost layer of RNME, which is the hydrophilic end of Rg3 that can form a hydrophilic layer on the surface of RNME, resulting in mutual repulsion with the hydrophilic layer of protein, thereby effectively decreasing protein adsorption and prolonging blood circulation. Effective prolongation of circulation in the bloodstream is closely related to tumor enrichment ability, which can increase tumor drug enrichment. Saline, Rg3, NPs, and RNME were injected into tumor-bearing mice *via* the tail vein, and the procedure used for the animal experiments is shown in Fig. S9.† The tumor size was measured *via* fluorescence imaging every 5 days, and it was found that the size did not significantly increase in the RNME group (Fig. S10†). Moreover, the fluorescence quantitative data showed that the tumor volume in the RNME group was significantly lower than that in other groups (Fig. 5C).

The body weights for the mice in each group were monitored for 21 days during the treatment process (Fig. 5D). Compared with the Ctrl and NPs groups, the weight of the Rg3 and RNME groups slightly increased, which indicates that Rg3 and RNME were nontoxic in pancreatic tumor mice. Then, the iron ion content of the main organs was measured by ICP-MS, and the biodistribution of the drug was studied. Compared with the saline group, the NP group exhibited obvious enrichment in the liver and spleen after 21 days of treatment, while there was only slight enrichment for the RNME group. It was confirmed that the outer layer protection of Rg3 prevented the premature leakage of iron ions, resulted in prolonged circulation in the blood, enhanced the EPR effect, and caused significant enrichment in the tumor sites in the RNME group (Fig. 5E). The average weight of each tumor group after 21 days of treatment and images of tumors are shown in Fig. 5F and G.

This phenomenon strongly confirmed the inhibitory effect of RNME. Compared with the control group that exhibited uncontrolled tumor growth within 21 days, there was inhibition of tumor growth by 32.6%, 28.1%, and 68.0% in the Rg3, NP, and RNME groups, respectively. This phenomenon is attributed to the fact that after Rg3 and NPs were administered alone, Rg3

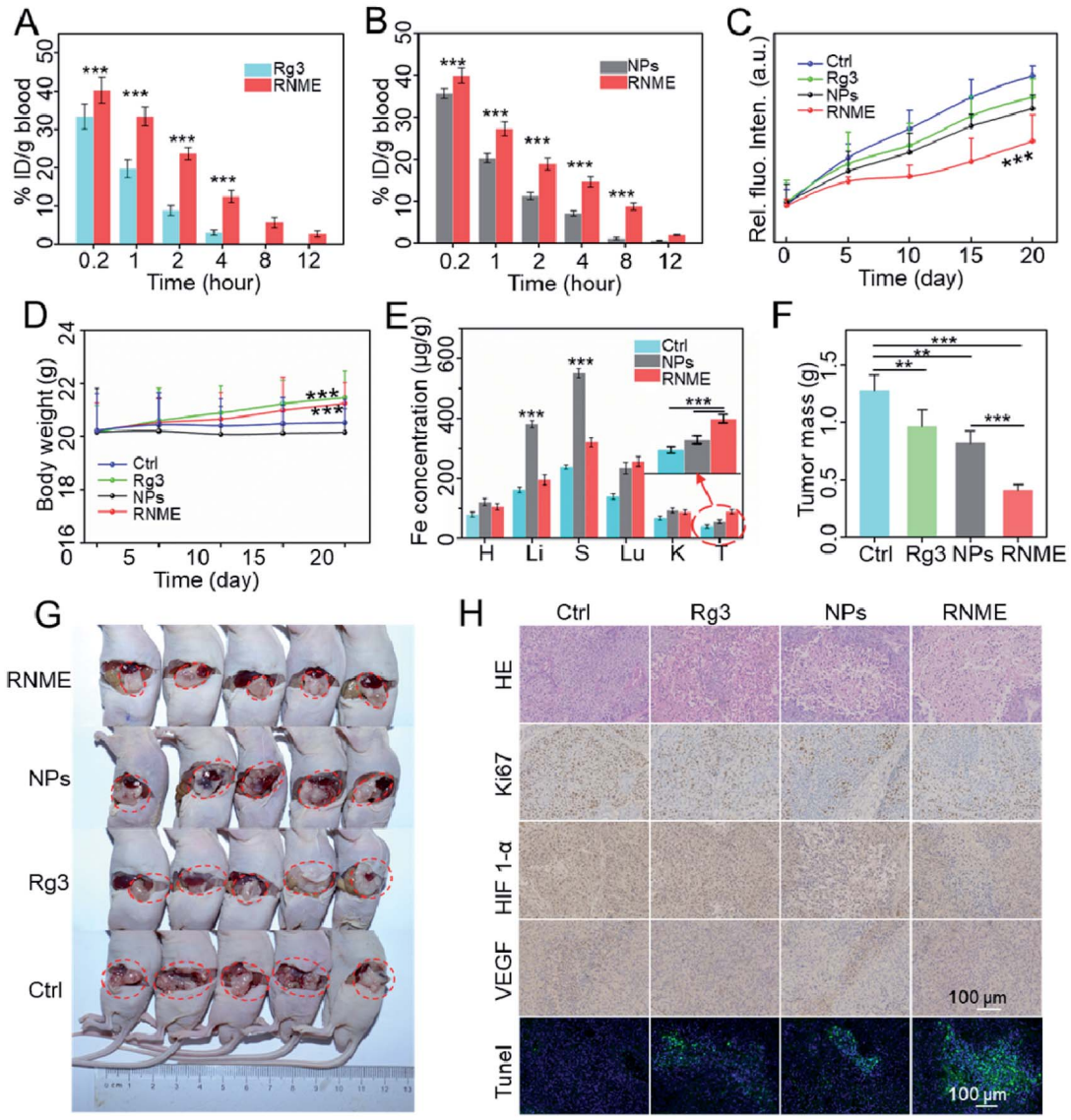

Fig. 5 Antitumor effects of the systemic administration of RNME. (A) The concentration of Rg3 *versus* time after the injection of Rg3 and RNME ($n = 3$). (B) The concentration of iron *versus* time after the injection of NPs and RNME ($n = 3$). (C) Quantitative values for bioluminescence imaging with different drug treatments. (D) Body weights of mice in different groups after 21 days. (E) Tissue distributions of iron measured *via* ICP-MS after NP and RNME treatment for 21 days. (F) The final weights of tumors after different drug treatments on day 21 ($n = 5$). (G) *In situ* imaging of tumors on day 21. (H) H&E, Ki67, HIF 1-α, VEGF, and TUNEL staining analysis assays of tumor tissue samples from different groups. All data are expressed as mean ± SD.

was quickly cleared in the blood, and a low amount of Rg3 could reach the tumor site compared with RNME. Due to instability in the blood, NPs may cause premature leakage of iron ions, resulting in toxic effects, and some of the NPs that reach the tumors have lost their catalytic activity. However, RNME can effectively prevent the leakage of iron ions, due to conjugation with Rg3. It maintains excellent catalytic activity and has a stronger EPR effect than NPs. After reaching the TME, controllable and sustained release of NMEs and Rg3 can be achieved due to the sensitivity of RNME to pH. Hence, after being released, with Rg3 activating cell apoptosis, NMEs simultaneously generate ROS in the tumor and activate apoptosis. Then, hematoxylin and eosin (H&E) staining, terminal deoxynucleotidyl transferase-mediated dUTP nick-end labeling (TUNEL) staining, and Ki67 staining of tumor tissues were performed. As shown in Fig. 5H, the H&E and TUNEL staining showed that compared with the other groups, the administration of RNME led to the highest level of apoptosis and necrosis in tumor tissues. In addition, Ki-67 staining showed a greater inhibition of cancer cell proliferation in the RNME group, which is consistent with the H&E and TUNEL staining results. This finding further indicated that RNME conferred an excellent synergistic antitumor effect. Compared with the PBS and Rg3 groups, the expression level of HIF-1α in

the NP and RNME groups significantly decreased, indicating that hypoxia at the tumor site increased. O_2 produced by H_2O_2 catalyzed by CAT-like activity reduced the tumor antioxidant capacity and increased the sensitivity of tumor cells to ROS, thereby increasing the therapeutic effect. Vascular endothelial growth factor (VEGF) staining revealed that RNME inhibited the expression of VEGF in a manner similar to that of Rg3.

In addition to the therapeutic effect, it was necessary to evaluate the possible occurrence of long-term toxicity. Then, 21 days after treatment, H&E staining of major organ (heart, liver, spleen, lung, and kidney) samples collected from mice was performed to assess the biocompatibility *in vivo*. There was no evident pathological toxicity in each group after treatment (Fig. S11†). Blood samples were also collected for serum biochemistry to measure the levels of alanine aminotransferase (ALT), aspartate transaminase (AST), lactate dehydrogenase (LDH), uric acid, blood urea nitrogen (BUN), creatine kinase (CK), creatinine, and creatine kinase-MB fraction (CK-MB) (Fig. S12†). Significantly enhanced concentrations of AST and ALT were measured in the NP group, which was caused by the enrichment of NPs in the liver. On the contrary, all values in the RNME group returned to the normal range. Therefore, the treatment was effective in preventing liver or other organ damage, and this showed that RNME is a safe and effective anticancer therapy. The abovementioned results demonstrated that RNME has great potential for use in the treatment of tumors.

Conclusions

We successfully designed a new type of nanodrug synthesized *via* coupling NMEs (heterostructures of metals and metal oxides) with Rg3. This guarantees the stability and safety of the internal NMEs, and it results in dual enzyme-like activity in the TME. A possible catalytic mechanism that can enhance POD- and CAT-like activity was proposed. The POD-like activity can catalyze the conversion of H_2O_2 into highly toxic ROS to kill tumor cells. The CAT-like activity can generate oxygen, inhibit hypoxia in the TME, reduce the antioxidant capabilities of tumor cells, and enhance oxidative damage. Then, an excellent synergistic effect against *in situ* pancreatic cancer was mediated by RNME combined with the anticancer effects of Rg3. After coupling, the metal–organic material significantly increased the utilization rate of Rg3, and the catalytic activity of RNME was fully demonstrated. Based on the obvious therapeutic effects, blood biochemistry tests and pathological analysis showed that RNME was completely safe. This research provides a new perspective relating to metal/metal oxide nanomaterials with excellent enzyme-like activity conjugated with organic pharmaceutical ingredients that can be applied to cancer treatment using a synergistic treatment strategy.

Author contributions

Xiaoxiong Zhao and Jicheng Wu: writing – writing original draft, investigation, data curation. Xiaoxiong Zhao, Jicheng Wu and Danjing Guo: formal analysis, data curation. Xiaoxiong Zhao, Liangjie Hong and Kaixin Zhang: investigation, methodology. Ben Wang: writing – review & editing. Xinhua Chen and Yujun Song: project administration, supervision, revising. All authors took part in data analysis and discussion.

Conflicts of interest

The authors declare no conflicts of interest.

Acknowledgements

This work was jointly supported by the National S&T Major Project of China (No. 2018ZX10301201), National Natural Science Foundation of China (No. 51971029, 81570168, 81401541, and 82027803), the BRICS STI Framework Program by NSFC (No. 51861145309), National Key R&D Program of China (No. 2018YFA0108603 and 2016YFC1100800), the Natural Science Foundation of Zhejiang Province (Nos. LR16H180001 and LY17H160016), ZJU Education Foundation (No. 2020XGZX06), and Major Consulting Projects of the Chinese Academy of Engineering (No. 2019-ZD-6-01).

Notes and references

1 H. Wei, L. Gao, K. Fan, J. Liu, J. He, X. Qu, S. Dong, E. Wang and X. Yan, *Nano Today*, 2021, **40**, 101269.
2 H. Wei and E. Wang, *Chem. Soc. Rev.*, 2013, **42**, 6060–6093.
3 J. Wu, X. Wang, Q. Wang, Z. Lou, S. Li, Y. Zhu, L. Qin and H. Wei, *Chem. Soc. Rev.*, 2019, **48**, 1004–1076.
4 Q. Liang, J. Xi, X. J. Gao, R. Zhang, Y. Yang, X. Gao, X. Yan, L. Gao and K. Fan, *Nano Today*, 2020, **35**, 100935.
5 R. Zhang, X. Yan and K. Fan, *Acc. Mater. Res.*, 2021, **2**, 534–547.
6 S. Gao, H. Lin, H. Zhang, H. Yao, Y. Chen and J. Shi, *Adv. Sci.*, 2019, **6**, 1801733.
7 K. Xu, X. Wu, Y. Cheng, J. Yan, Y. Feng, R. Chen, R. Zheng, X. Li, P. Song, Y. Wang and H. Zhang, *Nanoscale*, 2020, **12**, 23159–23165.
8 M. Liang and X. Yan, *Acc. Chem. Res.*, 2019, **52**, 2190–2200.
9 Z. Wang, R. Zhang, X. Yan and K. Fan, *Mater. Today*, 2020, **41**, 81–119.
10 L. Gao, K. Fan and X. Yan, *Theranostics*, 2017, **7**, 3207–3227.
11 G. Tang, J. He, J. Liu, X. Yan and K. Fan, *Exploration*, 2021, **1**, 75–89.
12 S. Zhao, X. Yu, Y. Qian, W. Chen and J. Shen, *Theranostics*, 2020, **10**, 6278–6309.
13 Z. Zhou, Y. Sun, J. Shen, J. Wei, C. Yu, B. Kong, W. Liu, H. Yang, S. Yang and W. Wang, *Biomaterials*, 2014, **35**, 7470–7478.
14 Z. Yang, Y. Luo, Y. Hu, K. Liang, G. He, Q. Chen, Q. Wang and H. Chen, *Adv. Funct. Mater.*, 2020, 2007991, DOI: 10.1002/adfm.202007991.
15 Z. Chen, J. J. Yin, Y. T. Zhou, Y. Zhang and N. Gu, *ACS Nano*, 2012, **6**, 4001–4012.
16 Y. Zhou, C. Liu, Y. Yu, M. Yin, J. Sun, J. Huang, N. Chen, H. Wang, C. Fan and H. Song, *Adv. Mater.*, 2020, **32**, e2003708.

17 Q. Chen, L. Feng, J. Liu, W. Zhu, Z. Dong, Y. Wu and Z. Liu, *Adv. Mater.*, 2016, **28**, 7129–7136.
18 L. Zhao, C. Fu, L. Tan, T. Li, H. Zhong and X. Meng, *Nanoscale*, 2020, **12**, 2855–2874.
19 B. Farran and G. P. Nagaraju, *Cytokine Growth Factor Rev.*, 2019, **48**, 11–23.
20 T. Kamisawa, L. D. Wood, T. Itoi and K. Takaori, *Lancet*, 2016, **388**, 73–85.
21 M. Reyngold, E. M. O'Reilly, A. M. Varghese, M. Fiasconaro, M. Zinovoy, P. B. Romesser, A. Wu, C. Hajj, J. J. Cuaron, R. Tuli, L. Hilal, D. Khalil, W. Park, E. D. Yorke, Z. Zhang, K. H. Yu and C. H. Crane, *JAMA Oncol.*, 2021, **7**(5), 735–738.
22 J. Jiang, Z. Yuan, Y. Sun, Y. Bu, W. Li and Z. Fei, *Biomed. Pharmacother.*, 2017, **96**, 619–625.
23 H. Lin, Y. Chen and J. Shi, *Chem. Soc. Rev.*, 2018, **47**, 1938–1958.
24 M. Li, H. Zhang, Y. Hou, X. Wang, C. Xue, W. Li, K. Cai, Y. Zhao and Z. Luo, *Nanoscale Horiz.*, 2020, **5**, 202–217.
25 Z. Peng, W. W. Wu and P. Yi, *Front. Pharmacol.*, 2020, **11**, 630825.
26 Z. Yuan, H. Jiang, X. Zhu, X. Liu and J. Li, *Biomed. Pharmacother.*, 2017, **89**, 227–232.
27 B. Zhou, Z. Yan, R. Liu, P. Shi, S. Qian, X. Qu, L. Zhu, W. Zhang and J. Wang, *Radiology*, 2016, **280**, 630–639.
28 T. G. Liu, Y. Huang, D. D. Cui, X. B. Huang, S. H. Mao, L. L. Ji, H. B. Song and C. Yi, *BMC Cancer*, 2009, **9**, 250.
29 Y. Cao, Q. Ye, M. Zhuang, S. Xie, R. Zhong, J. Cui, J. Zhou, Y. Zhu, T. Zhang and L. Cao, *PLoS One*, 2017, **12**, e0186520.
30 X. Liu, Z. Zhang, J. Liu, Y. Wang, Q. Zhou, S. Wang and X. Wang, *Int. Immunopharmacol.*, 2019, **72**, 98–111.
31 S. Kang, S. J. Park, A. Y. Lee, H. Jin, H. Y. Chung and D. S. Im, *J. Ginseng Res.*, 2018, **42**, 68–74.
32 Y. Zhu, J. Liang, C. Gao, A. Wang, J. Xia, C. Hong, Z. Zhong, Z. Zuo, J. Kim, H. Ren, S. Li, Q. Wang, F. Zhang and J. Wang, *J. Controlled Release*, 2020, **330**, 641–657.
33 L. Cheng, X. Sun, X. Zhao, L. Wang, J. Yu, G. Pan, B. Li, H. Yang, Y. Zhang and W. Cui, *Biomaterials*, 2016, **83**, 169–181.
34 X. Zhao, J. Wang, Y. Song and X. Chen, *Drug Dev. Ind. Pharm.*, 2018, **44**, 1307–1316.
35 S. Li, L. Shang, B. Xu, S. Wang and H. Liu, *Angew. Chem., Int. Ed.*, 2019, 131.
36 Z. Ren, X. Chen, L. Hong, X. Zhao, G. Cui, A. Li, Y. Liu, L. Zhou, R. Sun, S. Shen, J. Li, J. Lou, H. Zhou, J. Wang, G. Xu, Z. Yu, Y. Song and X. Chen, *Small*, 2019, **16**, e1905233.
37 Y. Song, S. Ji, Y.-J. Song, R. Li, J. Ding, X. Shen, R. Wang, R. Xu and X. Gu, *J. Phys. Chem. C*, 2013, **117**, 17274–17284.
38 J. Wang, Z. Wang, S. Li, R. Wang and Y. Song, *Nanoscale*, 2017, **9**, 4066–4075.
39 J. Wang, K. Zhao, X. Shen, W. Zhang, S. Ji, Y. Song, X. Zhang, R. Rong and X. Wang, *J. Mater. Chem. C*, 2015, **3**, 12418–12429.
40 X. Zhao, H. Liang, Y. Chen, X. Chen, W. Zhang, J. Wang, G. Zhang, V. I. Belotelov and Y. Song, *J. Mater. Chem. C*, 2021, **9**, 4619–4627.
41 W. Zhang, X. Zhao, Y. Yuan, F. Miao, W. Li, S. Ji, X. Huang, X. Chen, T. Jiang, D. A. Weitz and Y. Song, *Chem. Mater.*, 2020, **32**, 5044–5056.
42 L. Cui, A. M. Gouw, E. L. LaGory, S. Guo, N. Attarwala, Y. Tang, J. Qi, Y. S. Chen, Z. Gao, K. M. Casey, A. A. Bazhin, M. Chen, L. Hu, J. Xie, M. Fang, C. Zhang, Q. Zhu, Z. Wang, A. J. Giaccia, S. S. Gambhir, W. Zhu, D. W. Felsher, M. D. Pegram, E. A. Goun, A. Le and J. Rao, *Nat. Biotechnol.*, 2020, **39**, 357–367.
43 D. Wang, J. Zhou, R. Chen, R. Shi, G. Xia, S. Zhou, Z. Liu, N. Zhang, H. Wang, Z. Guo and Q. Chen, *Biomaterials*, 2016, **107**, 88–101.
44 Z. Gao, T. He, P. Zhang, X. Li, Y. Zhang, J. Lin, J. Hao, P. Huang and J. Cui, *ACS Appl. Mater. Interfaces*, 2020, **12**, 20271–20280.
45 X. Meng, D. Li, L. Chen, H. He, Q. Wang, C. Hong, J. He, X. Gao, Y. Yang, B. Jiang, G. Nie, X. Yan, L. Gao and K. Fan, *ACS Nano*, 2021, **15**, 5735–5751.